

Contents lists available at ScienceDirect

Displays

journal homepage: www.elsevier.com/locate/displa





Opto-mechanical design of Fourier transform spectral polarization imaging system based on dual Wollaston prisms *

Jingping Zhu*, Xiaofang Liu, Angze Li, Yue Liu*, Xun Hou

Key Laboratory for Physical Electronics and Devices of the Ministry of Education and Shaanxi Key Laboratory of Information Photonic Technique, Xi'an Jiaotong University, Xi'an 710049, China

ARTICLE INFO

Keywords:
Opto-mechanical design
Spectral
Polarization
Wollaston prisms
Phase modulation

ABSTRACT

The integration of polarization and spectral imaging, which exploits the principle of spectral interference, has long been a subject of extensive research. However, existing literature lacks comprehensive discussions on the opto-mechanical design of Fourier transform spectral polarization imaging systems (FTSPIS) employing dual Wollaston prisms (DWP). We proposing a novel opto-mechanical design strategy for FTSPIS based on DWP. Specifically, the FTSPIS system is divided into three independent modules: telescopic objective lens with phase modulation module (PMM), eyepiece and splitting system with DWP, and secondary imaging system. For each module, a detailed optimization design process is presented, with special emphasis on the optical effects produced by each module and their compatibility with one another. A practical design instance is provided to illustrate the feasibility of constructing a visible-spectrum FTSPIS that can achieve a full field of view (FOV) of \pm 5°. The effectiveness of the proposed design is verified through simulation analysis of interference patterns and demodulation. An elaboration on the mechanical structures for each module is also provided. These multidegree-of-freedom adjustment capabilities enable precise control of the system's performance, thus ensuring that the desired optical results can be achieved.

1. Introduction

Spectral imaging technology allows for the simultaneous acquisition of two-dimensional spatial intensity information and one-dimensional spectral data from a given target. The reflection, transmission and radiation spectra exhibited by various targets possess distinct characteristics, which, when analyzed, enable the classification and identification of these targets [1-4]. Similarly, polarization imaging technology captures both two-dimensional spatial intensity information and onedimensional polarization data from the target concurrently [5]. This technology demonstrates a significantly enhanced sensitivity for features such as the target's roughness, surface structure, contour nuances, humidity levels, and more. And the polarization characteristics of various materials diverge significantly [6], a trait that can be harnessed for the contour enhancement of targets and classification and identification of substances [7-15]. In recent years, polarization imaging has significantly expanded its scope, finding applications in the emerging field of imaging targets within turbid media [16-19]. The integration of polarization and spectral multidimensional optical information greatly enhances its versatility and strengthens detection capabilities, leading to its applications in various fields such as geological monitoring [20,21], environmental remote sensing [22–26], biomedicine [27–31], agricultural production [32–36], and numerous other endeavors [37,38].

Based on the spectroscopic mode of the instrument, spectral polarimetric imaging techniques can be classified into five categories: filterbased [39], dispersive [40–42], computational tomography-driven [43–47], coded aperture-utilizing [48–52], and interferometric approaches. Interferometric spectral imaging technology exploits the relationship between interference intensity and spectral intensity in information optics to reconstruct spectral profiles. By applying an inverse Fourier transform to the interference patterns captured by the camera, this method enables precise spectral recovery. It offers several advantages, including high spectral resolution, a broad spectral range, compact size, structural simplicity, and exceptional stability. Consequently, it has garnered significant attention from the academic community in recent years. Mu et al [53] proposed a novel hyperspectral polarization imaging technique. This system employs a Savart plate to introduce an optical path difference and operates on a spatio-temporal

E-mail addresses: jpzhu@xjtu.edu.cn (J. Zhu), 18792666707@163.com (Y. Liu).

 $[\]ensuremath{^{\star}}$ This paper was recommended for publication by Prof Guangtao Zhai.

^{*} Corresponding authors.

Fig. 1. Schematic of the FTSPIS. FTSPIS can be divided into three core modules: telescopic objective lens with phase modulation module (PMM), eyepiece and splitting system with dual Wollaston prisms (DWP), and secondary imaging system.

hybrid modulation principle, integrating the aperture-division polarization detection technique. Specifically, the Savart plate-based interferometric spectral imaging system utilizes a DWP to split the incident imaging beam, thereby eliminating the need for a PMM. By leveraging a single detector, the system can simultaneously capture four sets of linear polarization interference patterns, though it is incapable of detecting circular polarization information. The system's FOV along the x-axis is \pm 3°, whereas along the y-axis, it is limited to \pm 0.7°. Bai et al [54] initially proposed a hyperspectral imaging system, and the following year, they further developed a time-sharing hyperspectral polarization imaging system based on liquid crystal modulation [55]. This system utilizes a Wollaston prism combined with a corner cube retroreflector for spectral beam splitting and interference. Polarization modulation is achieved through the use of ferroelectric liquid crystals and linear polarizers. By rapidly switching the fast-axis orientation of the ferroelectric liquid crystals, the system enables efficient time-multiplexed detection of full-Stokes polarization information. Yan et al [56] introduced a hyperspectral resolution channel modulation spectropolarimetry imaging technique that utilizes a liquid crystal variable retarder. This system employs a Savart plate for spectral beam splitting and optical path difference generation. By controlling the retardation of the liquid crystal retarder, it captures interference patterns from different polarization channels in a time-multiplexed manner. The system offers high spectral resolution and large optical throughput. Additionally, the liquid crystal variable retarder is computer-controlled, and with a design free of moving parts, the system remains compact, structurally stable, and highly reliable. Li et al. [57] proposed a channel modulation-based hyperspectral polarization imaging system utilizing Wollaston prisms. This system integrates a sub-aperture polarization detection technique, utilizing two Wollaston prisms with orthogonal optical axes to simultaneously segment the FOV and differentiate polarization states. This design effectively suppresses crosstalk in channel modulation interferograms. With its simple, compact, and highly stable structure, the system enables comprehensive polarization detection. Bai et al. [58] proposed a static Fourier transform full-spectrum polarization imaging system that combines a liquid crystal polarization modulator and a birefringent shearing interferometer. The liquid crystal polarization modulator utilizes two ferroelectric liquid crystals and two wave plates to generate four polarization states, enabling high-speed time-division capturing of full-Stokes polarization images with high signal-to-noise ratios. The birefringent shearing interferometer consists of two birefringent crystal plates, achieving a maximum FOV of \pm 5°.

The FTSPIS, based on a DWP, integrates prism-based dispersive spectroscopy with full-Stokes polarization imaging, enabling the simultaneous acquisition of both spectral and polarization data form target signatures. In this system, the PMM encodes the Stokes vector components into spectrally resolved interference patterns via coherent superposition, facilitating single-shot polarimetric-spectral imaging at video rates. Notably, the DWP configuration within the interferometric subassembly offers two key advantages over conventional single

Wollaston prism designs: (1) enhanced optical path parallelism through symmetrical beam splitting and (2) improved phase stability during polarization state modulation.

We propose a design and analysis methodology for the FTSPIS, rigorously verifying the pivotal modules through optical analyses. The methodology systematically progresses through four critical phases: (1) modular optical subsystem optimization, (2) full-system aberration balancing, (3) opto-mechanical integration verification, and (4) system-level performance validation. Ultimately, the system is subjected to rigorous testing and verification, validating the robustness and efficacy of our proposed approach. The structure of this study is as follows: The structure and basic physical principle of the FTSPIS are detailed in section 2. The optical design and analysis of the optimization are illustrated in section 3. The simulation verification is conducted in section 4. The design and analysis of the opto-mechanical structures are presented in section 5.

2. Basic principle of FTSPIS

This section provides a detailed explanation of the physical principles underlying the FTSPIS system, serving as a theoretical foundation for the system design methods introduced in the subsequent sections.

2.1. The structure and function of FTSPIS

The optical schematic of the proposed FTSPIS is depicted in Fig. 1. The system consists of a front optical assembly, represented by two gray lenses, which serves as the entry point for incoming light. Subsequently, the system incorporates two phase retarders (designated as R_1 and R_2), a pair of polarizers (P_1 and P_2), and a DWP for light separation. The DWP consists of two identical Wollaston prisms with an adjustable air gap of width s between them, an imaging lens (L) for focusing, and finally, a CMOS detector for image acquisition.

The incoming light, which is normally incident monochromatic light, is modulated by the PMM, encoding the original polarization information into the intensity component of the outgoing light. The modulated light is then sheared by the DWP into two identical, parallel polarized beams, which are subsequently focused by L and image onto the light-sensitive surface of the CMOS camera.

A crucial component of the FTSPIS is the PMM, which is constructed from R_1 , R_2 and P_1 . Meanwhile, the DWP serves as the cornerstone of the interference module, facilitating the creation of interference patterns essential for imaging. The key optical orientations are illustrated in Fig. 1, including the polarizing directions of P_1 and P_2 , the fast axis directions of P_1 and P_2 , and the optical axis directions of each wedge within the DWP. Notably, the thickness of the phase retarders P_1 and P_2 is deliberately designed, with P_1 and P_2 being their respective dimensions, maintaining a ratio of 1:2.

Table 1Design index parameters of FTSPIS.

Index	Parameters
Focal length of telescopic objective system	120 mm +5°
Thickness of phase retarders	R ₁ (4.85 mm), R ₂ (9.7 mm)
Thickness of polarizers	8 mm
Thickness of Wollaston prisms	10.2 mm
Focal length of secondary imaging system	50 mm
The image height of FTSPIS	$h \geq 14.05 \; mm$

2.2. Physical principle of phase modulation module

The light from the object is collected and collimated by the front optical system, while the polarization information undergoes modulation via the PMM. The phase retarders, made from uniaxial crystals in the form of parallel flat plates, have optical axes precisely aligned parallel to the crystal interface. The retardation of R_1 and R_2 can be

mathematically expressed as follows [59]:

$$\begin{cases} \varphi_1 = \frac{2\pi}{\lambda} (n_e - n_0) d_1 \\ \varphi_2 = \frac{2\pi}{\lambda} (n_e - n_0) d_2 \end{cases}$$
 (1)

Where λ represents the wavelength, n_0 and n_e denote the refractive indexes corresponding to the ordinary (o) and extraordinary (e) light rays, respectively. The values of n_0 and n_e for calcite at varying wavelengths are accurately derived utilizing the Sellmeier formula. The Mueller matrix of an ideal retarder, distinguished by its specific retardation of φ and the fast axis angle of θ , is formulated as follows:

$$M_{R} = \begin{bmatrix} 1 & 0 & 0 & 0\\ 0 & \cos^{2}2\theta + \sin^{2}2\theta\cos\varphi & (1 - \cos\varphi)\sin2\theta\cos2\theta & -\sin\varphi\sin2\theta\\ 0 & (1 - \cos\varphi)\sin2\theta\cos2\theta & \sin^{2}2\theta + \cos^{2}2\theta\cos\varphi & \sin\varphi\cos2\theta\\ 0 & \sin\varphi\sin2\theta & -\sin\varphi\cos2\theta & \cos\varphi \end{bmatrix}$$

$$(2)$$

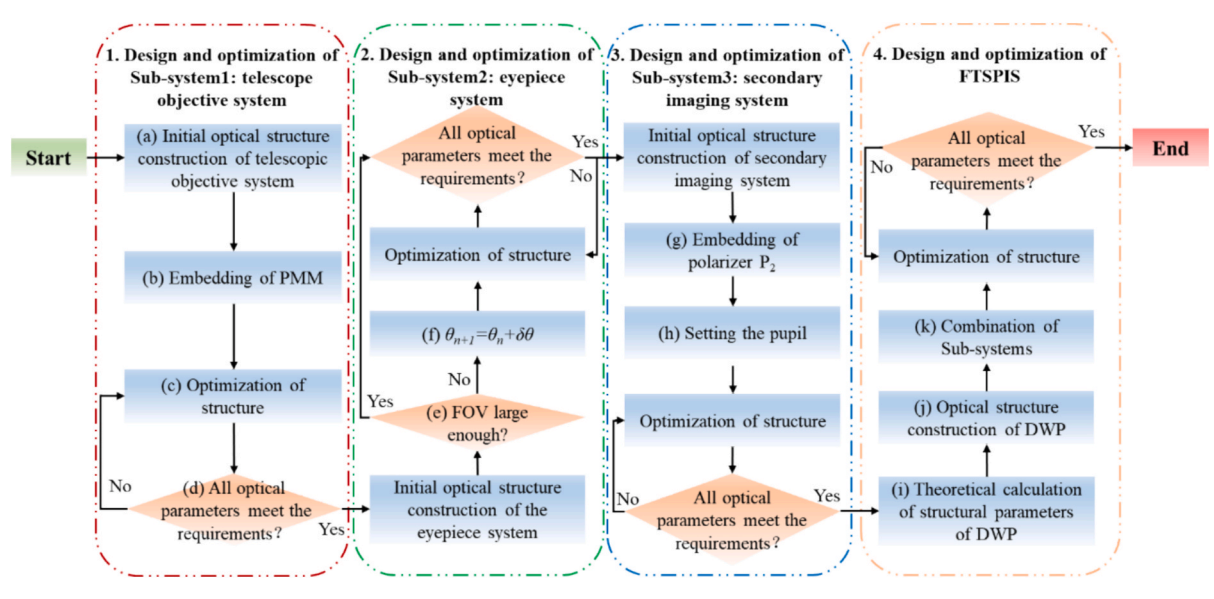


Fig. 2. Optical design procedures of FTSPIS.

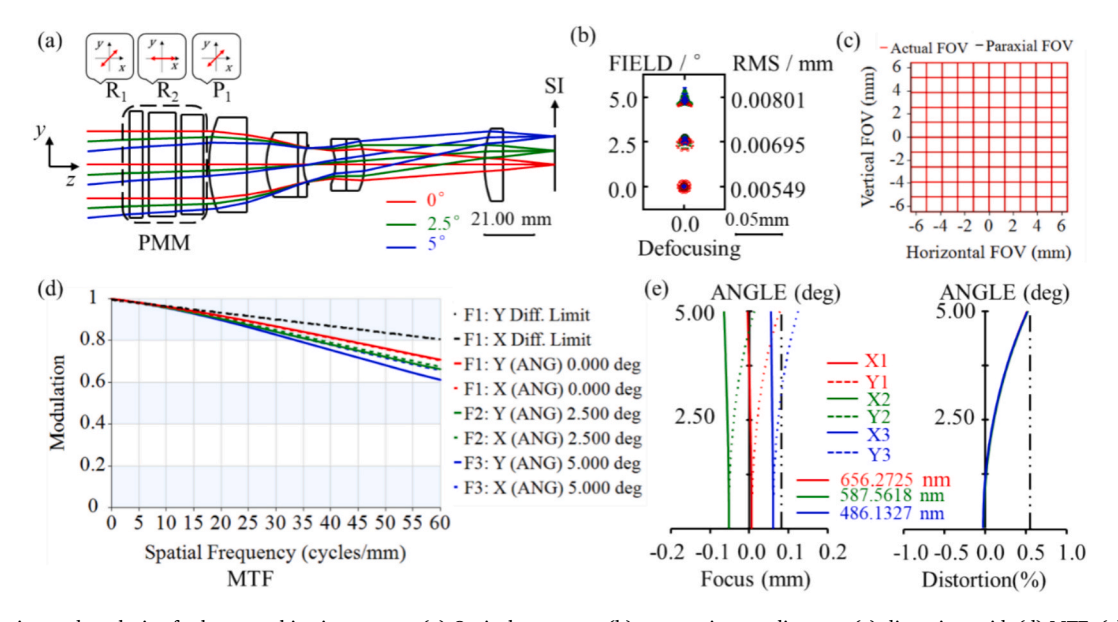


Fig. 3. Optimization and analysis of telescope objective system. (a) Optical structure, (b) geometric spot diagram, (c) distortion grid, (d) MTF, (e) field curves of optimized system.

 $\begin{tabular}{ll} \textbf{Table 2} \\ \textbf{The structure and surface parameters of the optimized telescope objective system.} \end{tabular}$

Surface	Y Radius/mm	Thickness/mm	Materials
S0	infinite	infinite	
S1	infinite	4.85	Quartz
S2	infinite	2.00	
S3	infinite	9.70	Quartz
S4	infinite	2.00	
S5	infinite	8.00	NBK7_SCHOTT
S6	infinite	2.00	
S7	44.42	13.56	HZK4_CDGM
S8	Infinite	6.54	
S9	25.79	11.47	HZK3_CDGM
S10	infinite	2.27	HZF5_CDGM
S11	17.29	1.60	
S12	infinite	9.25	
S13	-18.03	3.40	HZBAF21_CDGM
S14	infinite	6.06	HZF2_CDGM
S15	-22.57	31.08	
S16	39.99	9.74	HQK3L_CDGM
S17	infinite	21.01	
SI	infinite	0.00	

The Mueller matrix of an ideal polarizer, with its polarization angle denote as θ , can be expressed in the following mathematical form:

$$M_{P} = \frac{1}{2} \begin{bmatrix} 1 & \cos 2\theta & \sin 2\theta & 0\\ \cos 2\theta & \cos^{2} 2\theta & \sin 2\theta \cos 2\theta & 0\\ \sin 2\theta & \sin 2\theta \cos 2\theta & \sin^{2} 2\theta & 0\\ 0 & 0 & 0 & 0 \end{bmatrix}$$
(3)

The total Mueller matrix of the PMM can be systematically derived through the multiplication of the individual Mueller matrices corresponding to each constituent component:

$$M_{PMM} = M_{P_1} \cdot M_{R_2} \cdot M_{R_1}$$

$$= \frac{1}{2} \begin{bmatrix} 1 & \sin\varphi_1 \sin\varphi_2 & \cos\varphi_2 & \cos\varphi_1 \sin\varphi_2 \\ 0 & 0 & 0 & 0 \\ 1 & \sin\varphi_1 \sin\varphi_2 & \cos\varphi_2 & \cos\varphi_1 \sin\varphi_2 \\ 0 & 0 & 0 & 0 \end{bmatrix}$$
(4)

The relationship between the Stokes parameters of the input and output light from the PMM can be characterized as:

$$S'(x, y, \sigma) = M_{PMM} \cdot S(x, y, \sigma)$$

$$=\frac{1}{2}\begin{bmatrix} S_{0}+S_{1}\sin\varphi_{1}\sin\varphi_{2}+S_{2}\cos\varphi_{2}+S_{3}\cos\varphi_{1}\sin\varphi_{2}\\ 0\\ S_{0}+S_{1}\sin\varphi_{1}\sin\varphi_{2}+S_{2}\cos\varphi_{2}+S_{3}\cos\varphi_{1}\sin\varphi_{2}\\ 0 \end{bmatrix} = \begin{bmatrix} S_{0}\\ S_{1}\\ S_{2}\\ S_{3} \end{bmatrix}$$
(5)

Where the S_0 - S_3 represent the Stokes parameters of the input light, whereas the S' $_0$ -S' $_3$ signify the Stokes parameters of the output light after passing through the PMM. It can be seen that the input Stokes parameters has been fully modulated by the PMM to the first term of the output Stokes parameters, the coefficient is intimately linked to the retardation of phase retarders. This indicates that the original polarization information has been modulated to different channels.

2.3. Physical principle of the interference module

The interference module is inherently a sophisticated device, functioning as an interference spectrometer. Given that the polarization states of the two lights it separates are different, the Mueller matrices M_W of the two lights should be discussed separately. The output light is then separate into two parallel lights by the DWP, which are orthogonally polarized in the direction of polarization. For two separation lights, the Mueller matrix M_W of the DWP can be analytically approximated to two orthogonal line polarizers with polarization directions in the horizontal and vertical directions. This Mueller matrix calculated according to the Equation (1.3) and expressed as:

Table 3The structure and surface parameters of the optimized eyepiece system.

Surface	Y Radius/mm	Thickness/mm	Materials
S0	infinite	infinite	
S1	infinite	29.50	
S2	infinite	5.00	ZF3_CDGM
S3	33.71	7.14	HZK3_CDGM
S4	-34.75	7.70	
S5	28.10	5.00	NBK7_SCHOTT
S6	49.20	32.29	
SI	infinite	0.00	

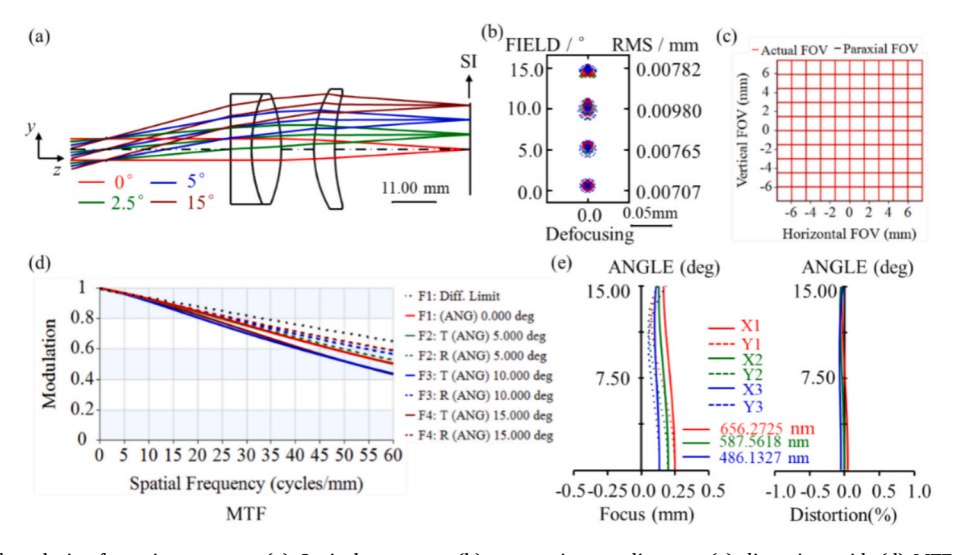


Fig. 4. Optimization and analysis of eyepiece system. (a) Optical structure, (b) geometric spot diagram, (c) distortion grid, (d) MTF, (e) field curves of optimized system.

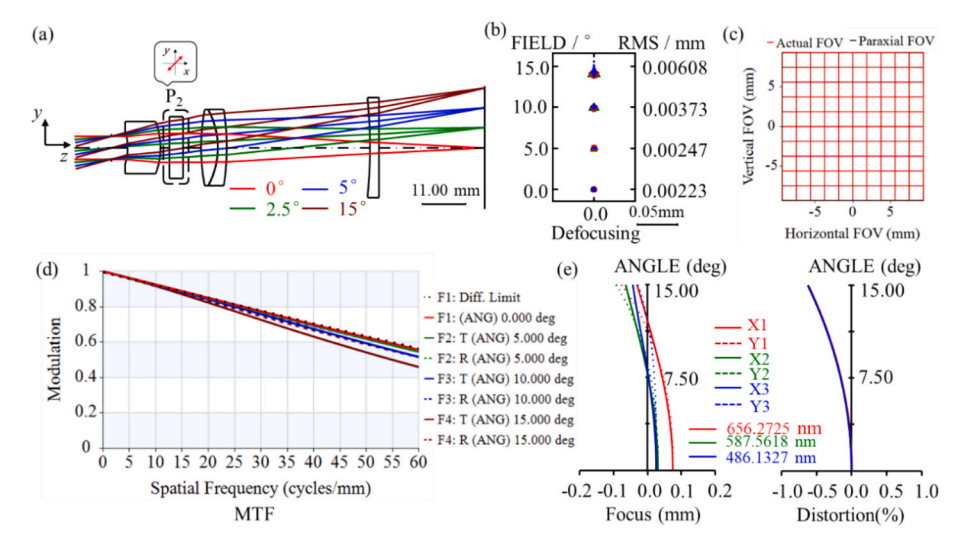


Fig. 5. Optimization and analysis of secondary imaging system. (a) Optical structure, (b) geometric spot diagram, (c) distortion grid, (d) MTF, (e) field curves of optimized system.

Table 4The structure and surface parameters of the optimized secondary imaging system.

Surface	Y Radius/mm	Thickness/mm	Materials
S0	infinite	infinite	
S1	infinite	1.00	
S2	infinite	2.45	
S3	-12.39	7.22	HZBAF50_CDGM
S4	-15.48	2.00	
S5	infinite	3.00	NBK7_SCHOTT
S6	infinite	2.00	
S7	infinite	2.00	
S8	51.89	3.27	HZK14_CDGM
S9	-17.45	2.00	HZF6_CDGM
S10	-52.95	31.44	
S11	-106.80	2.00	HLAK11_CDGM
S12	infinite	23.23	
SI	infinite	0.00	

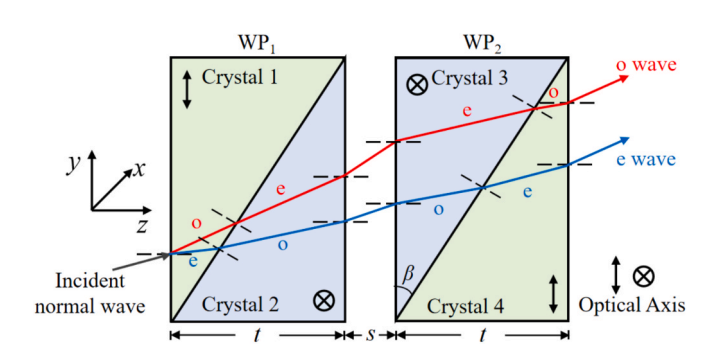


Fig. 6. Optical path for DWP: a normal incident wave can be split into two parallel waves o (red) and e (blue).

Then the relationship between the Stokes parameters output from the DWP and the Stokes parameters output from the PMM is:

$$\begin{bmatrix} S_{0W_{1}}^{\prime}(\sigma) \\ S_{1W_{1}}^{\prime}(\sigma) \\ S_{2W_{1}}^{\prime}(\sigma) \\ S_{3W_{1}}^{\prime}(\sigma) \end{bmatrix} = \frac{1}{4} \begin{bmatrix} S_{0} + S_{1}\sin\varphi_{1}\sin\varphi_{2} + S_{2}\cos\varphi_{2} + S_{3}\cos\varphi_{1}\sin\varphi_{2} \\ S_{0} + S_{1}\sin\varphi_{1}\sin\varphi_{2} + S_{2}\cos\varphi_{2} + S_{3}\cos\varphi_{1}\sin\varphi_{2} \\ 0 \\ 0 \end{bmatrix}$$
(8)

$$\begin{bmatrix} S_{0W_{2}}(\sigma) \\ S_{1W_{2}}(\sigma) \\ S_{2W_{2}}(\sigma) \\ S_{3W_{2}}(\sigma) \end{bmatrix} = \frac{1}{4} \begin{bmatrix} S_{0} + S_{1} \sin\varphi_{1} \sin\varphi_{2} + S_{2} \cos\varphi_{2} + S_{3} \cos\varphi_{1} \sin\varphi_{2} \\ -S_{0} - S_{1} \sin\varphi_{1} \sin\varphi_{2} - S_{2} \cos\varphi_{2} - S_{3} \cos\varphi_{1} \sin\varphi_{2} \\ 0 \\ 0 \end{bmatrix}$$
(9)

The first term of the Stokes parameters for the two light beams from the DWP is identical, indicating that both beams have the same light intensity and carry congruent intensity information. The second term, with opposite signs and equal magnitudes, reveals that the polarization directions of the two beams are mutually orthogonal.

Then after the polarizer P_2 , the Stokes parameters of the two output lights are respectively:

$$\begin{bmatrix} S_{0p_{1}}'(\sigma) \\ S_{1p_{1}}'(\sigma) \\ S_{2p_{1}}'(\sigma) \\ S_{3p_{1}}'(\sigma) \end{bmatrix} = \frac{1}{8} \begin{bmatrix} S_{0} + S_{1} \sin\varphi_{1} \sin\varphi_{2} + S_{2} \cos\varphi_{2} + S_{3} \cos\varphi_{1} \sin\varphi_{2} \\ 0 \\ S_{0} + S_{1} \sin\varphi_{1} \sin\varphi_{2} + S_{2} \cos\varphi_{2} + S_{3} \cos\varphi_{1} \sin\varphi_{2} \\ 0 \\ 0 \end{bmatrix}$$
(10)

$$\begin{bmatrix} S_{0p_2}''(\sigma) \\ S_{1p_2}''(\sigma) \\ S_{2p_2}''(\sigma) \\ S_{3p_2}''(\sigma) \end{bmatrix} = \frac{1}{8} \begin{bmatrix} S_0 + S_1 \sin\varphi_1 \sin\varphi_2 + S_2 \cos\varphi_2 + S_3 \cos\varphi_1 \sin\varphi_2 \\ 0 \\ S_0 + S_1 \sin\varphi_1 \sin\varphi_2 + S_2 \cos\varphi_2 + S_3 \cos\varphi_1 \sin\varphi_2 \\ 0 \\ 0 \end{bmatrix}$$
(11)

It can be observed that the intensity and polarization information of the two beams passing through the polarizer P_2 are identical, with their amplitudes being equal. Since the polarization states of the two beams emanating from polarizer P_2 are congruent, they interfere on the CMOS photosensitive surface, resulting in the formation of an image with an interference pattern. To capture the complete interference information of FTSPIS, a scanning process is required to change the angle and the optical path difference (OPD), thereby the full spectrum of interference information from the target.

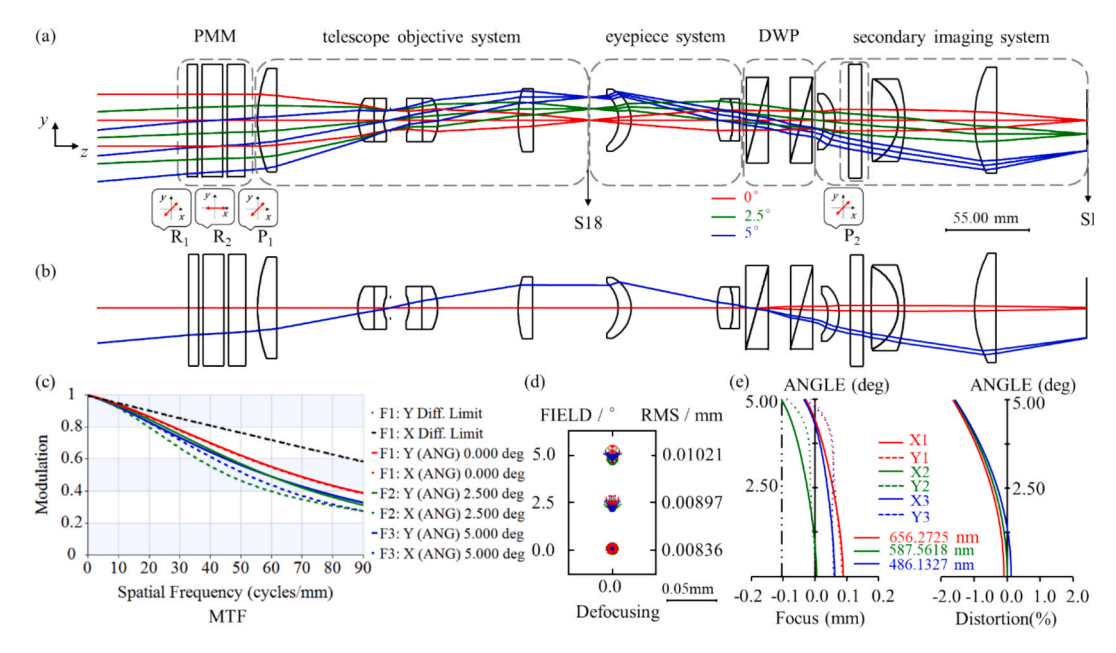


Fig. 7. Optimization and analysis of FTSPIS. (a) Optical structure, (b) schematic diagram of light propagation and separation, (c) MTF, (d) geometric spot diagram, (e) field curves of optimized system.

Table 5The structure and surface parameters of the optimized FTSPIS.

Surface	Y Radius/mm	Thickness/mm	Materials
S0	infinite	infinite	
S1	infinite	4.85	Quartz
S2	infinite	2.00	·
S3	infinite	9.70	Quartz
S4	infinite	2.00	
S5	infinite	8.00	NBK7_SCHOTT
S6	infinite	6.00	
S7	71.66	11.80	HZK4_CDGM
S8	427.57	61.03	
S9	20.57	7.97	HZK3_CDGM
S10	-52.02	4.87	HZF5_CDGM
S11	12.06	6.00	
S12	infinite	6.00	
S13	-17.50	5.53	HZBAF21_CDGM
S14	20.65	8.78	HZF2_CDGM
S15	-20.95	38.95	
S16	63.18	7.96	HQK3L_CDGM
S17	-150.02	34.19	
S18	infinite	21.95	
S19	-20.00	6.78	HLAF3B_CDGM
S20	-18.86	38.78	
S21	34.94	6.93	HLAK10_CDGM
S22	-40.00	3.00	HZBAF21_CDGM
S23	-319.45	6.00	
S24	infinite	5.10	Calcite
S25	infinite	5.10	Calcite
S26	infinite	10.00	
S27	infinite	5.10	Calcite
S28	infinite	5.10	Calcite
S29	infinite	6.00	
S30	-11.39	6.00	HQK3L_CDGM
S31	-14.67	26.28	
S32	infinite	6.00	NBK7_SCHOTT
S33	infinite	26.28	
S34	240.66	17.93	HLAK10_CDGM
S35	-29.23	3.00	HQK3L_CDGM
S36	-95.27	9.85	
S37	50.34	13.16	HZBAF21_CDGM
S38	infinite	48.85	
S39	infinite	0.00	

intensity I_0 , which is precisely equal to the first row of the Stokes parameters characterizing the output light's polarization state.

$$I_{0} = \frac{1}{8}(S_{0} + S_{1}\sin\varphi_{1}\sin\varphi_{2} + S_{2}\cos\varphi_{2} + S_{3}\cos\varphi_{1}\sin\varphi_{2})$$
 (12)

In practical applications, the incident light is primarily polychromatic, spanning a broad spectrum of wavelengths. Consequently, the observed interference intensity is the superposition of individual interference intensities from each wavelength within the spectral range, all occurring at the same OPD. The two light beams through lenses positioned in the focal plane of the detector, where they form an interference pattern. The corresponding light intensity, as measured by the detector and captured in the interferogram, is expressed as:

$$\begin{split} I(\Delta) &= \frac{1}{8} \int_{\sigma_1}^{\sigma_2} (S_0 + S_1 \sin\varphi_1 \sin\varphi_2 + S_2 \cos\varphi_2 + S_3 \cos\varphi_1 \sin\varphi_2) d\sigma \\ &+ \frac{1}{8} \int_{\sigma_1}^{\sigma_2} (S_0 + S_1 \sin\varphi_1 \sin\varphi_2 + S_2 \cos\varphi_2 + S_3 \cos\varphi_1 \sin\varphi_2) \cos(2\pi\sigma\Delta) d\sigma \end{split} \tag{13}$$

Where $I(\Delta)$ is final interference intensity, σ is the wavenumber, and Δ is the OPD, which is related to the thickness s of the air gap. The equation of Δ has been thoroughly analyzed using the wave normal tracing method in our previous work [60].

3. Optical design and analysis of FTSPIS

The FTSPIS consists of a telescope objective system, an eyepiece system and a secondary imaging system. Therefore, considering the design concept of sub-total, it is necessary to design the high-resolution front telescope objective system (while embedding the designed PMM), eyepiece system, and secondary imaging system (while embedding the DWP). Additionally, the performance of each imaging subsystem must be analyzed individually to ensure proper subsystem matching and to achieve joint system optimization. Based on this analysis and the relevant project requirements, the optical system parameters for the polarization interference imaging system are provided in Table 1.

The detector's capabilities are confined to perceiving the light

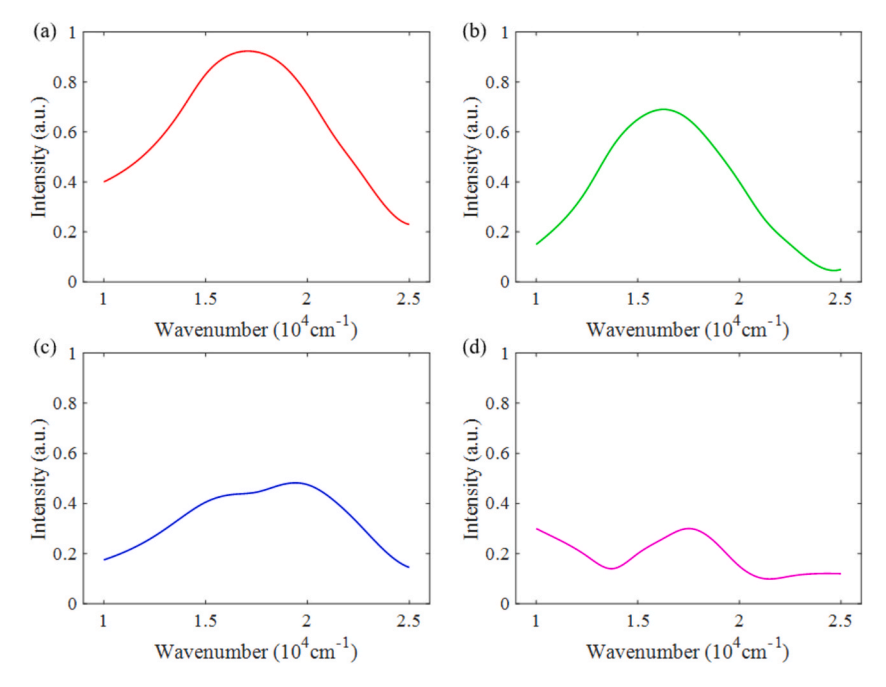


Fig. 8. Original Stokes polarization spectrum. (a) Stokes vector S_0 parameter, (b) Stokes vector S_1 parameter, (c) Stokes vector S_2 parameter, (d) Stokes vector S_3 parameter.

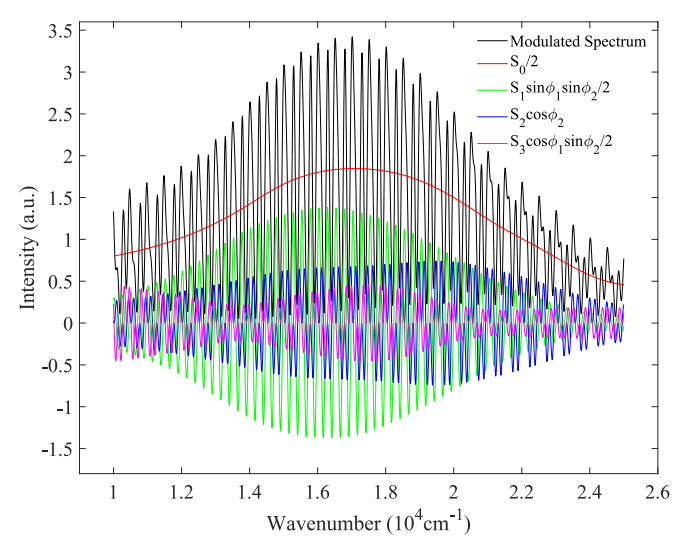


Fig. 9. Intensity spectrum components of Stokes parameters after modulation module.

3.1. Optical design basic procedures for FTSPIS

As shown in Fig. 2, the optical design procedures of FTSPIS can be illustrated as follows:

- (a) Initial optical structure construction of telescopic objective system. When selecting the initial structure, preference should be given to structures that are close to the FOV and effective focal length required by the design. As the initial structure of the telescope objective system, the double-Gauss objective lens is ultimately selected.
- (b) Embedding of PMM. During the design of the telescopic objective system, the PMM (two phase retarders R₁ and R₂, and polarizer P₁) is embedded at the same time, and it is ensured that the three elements are always kept in a parallel glass plate structure with a

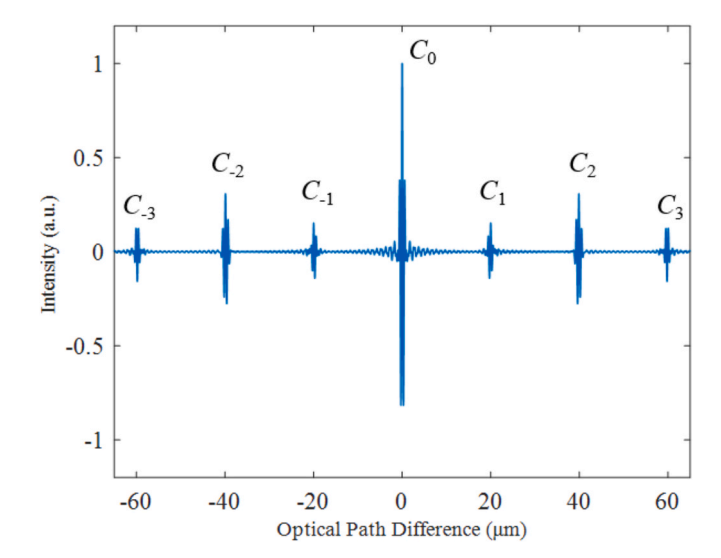


Fig. 10. Seven-channel interference intensity curve of FTSPIS.

fixed constant thickness during the design and optimization process.

(c) Optimization of structure. In the optimization, the optimization variables are corresponding to the thickness, Y radius and material of each lens. In the structure optimization of FTSPIS (the orange dashed-line box), the structural angle of the DWP is set as an additional variable. The constraints correspond to the edge and center thicknesses of the lens, which initially ensure the manufacturability of the designed lenses while maintaining high image quality. Additionally, specific constraints, such as the desired focal length, are imposed. To facilitate the integration of the telescope objective system with the eyepiece system, it is necessary to constrain the image height and the angle of incident light at the image plane. The detailed optimization process will be outlined in the following sections.

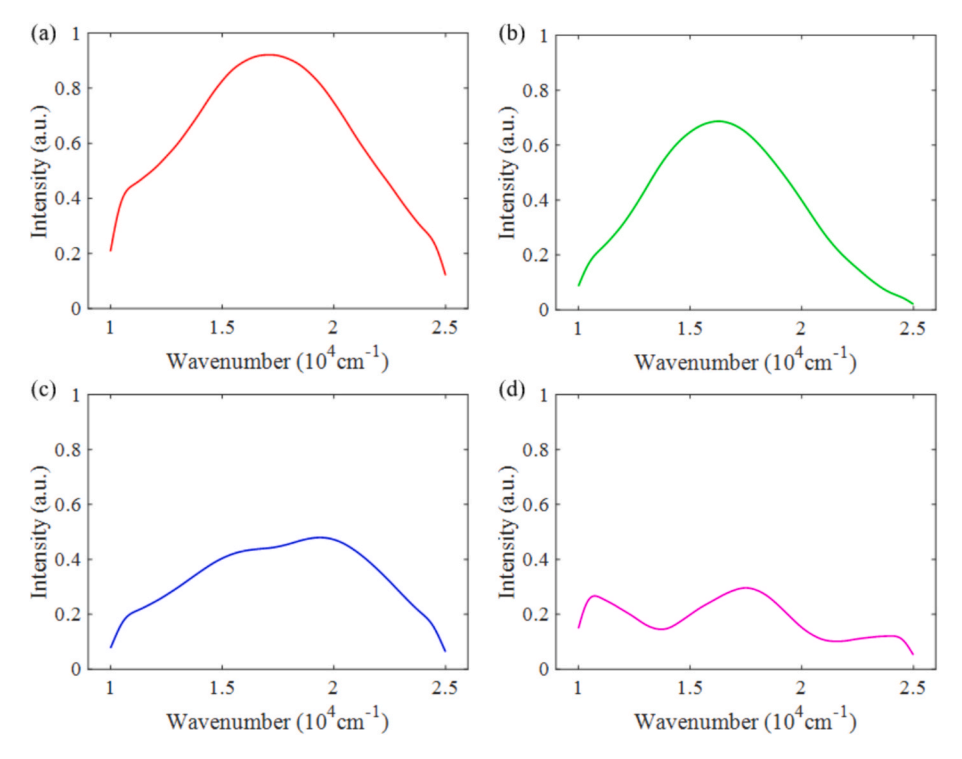


Fig. 11. Recovered Stokes polarization spectrum. (a) Recovered Stokes vector S_0 parameter, (b) Recovered Stokes vector S_1 parameter, (c) Recovered Stokes vector S_2 parameter, (d) Recovered Stokes vector S_3 parameter.

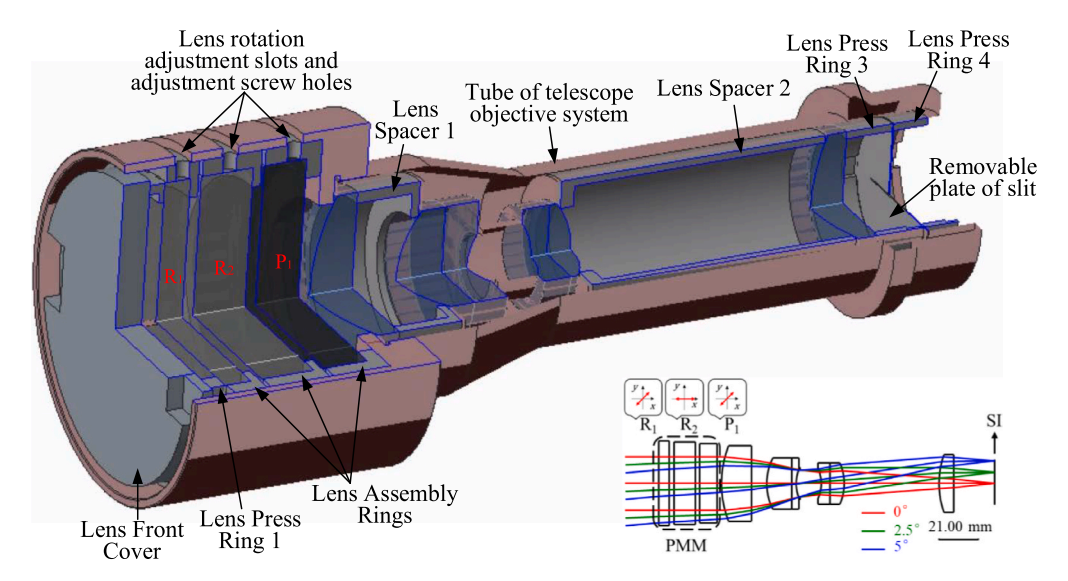


Fig. 12. Opto-mechanical structure of telescopic objective system with PMM modules R₁, R₂, and P₁.

- (d) All optical parameters meet the requirements? To ensure optimal performance when connecting the telescope objective system and eyepiece system, it is crucial to match the image height and exit pupil between the two systems. Furthermore, it is essential to verify that the RMS diameters across all four systems meet the specified requirements. If any parameter fails to meet the desired criteria, the optimization process must continue until all parameters are successfully aligned with the desired specifications.
- (e) FOV large enough. The eyepiece system is designed in reverse, as is typical in optical designs where the object and image planes of the eyepiece are in reversed positions, as defined by optical software. This reversal allows the eyepiece to be matched with the objective lens. Based on the FOV and image height of the
- telescope objective system and the magnification requirement of the front telescopic system, the eyepiece is further optimized and the desired FOV of eyepiece is obtained.
- (f) $\theta_{n+1}=\theta_n+\delta\theta$. In multiple optimization cycles, to ensure that the system can be imaged properly, the FOV should be enlarged gradually until it reaches the desired value.
- (g) Embedding of polarizer P₂. The polarizer P₂ is integrated into the secondary imaging system, ensuring that it consistently maintains a parallel glass plate structure with a fixed thickness throughout the design and optimization process.
- (h) Setting the pupil. In the design and optimization of secondary imaging system, the pupil of the secondary imaging system should be designed to match the pupil of the eyepiece system.

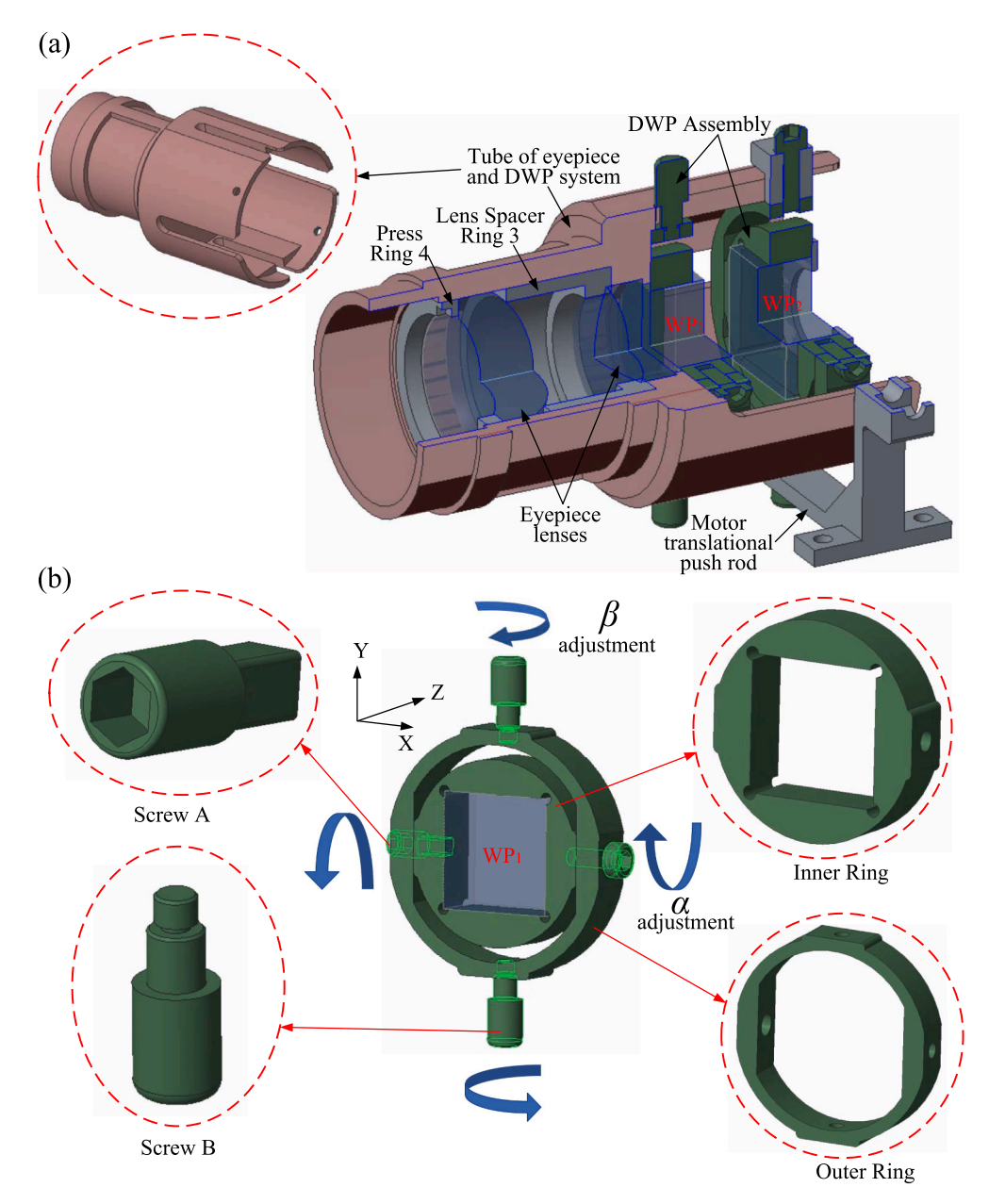


Fig. 13. Opto-mechanical structure for eyepiece system and DWP assembly system. (a) Sub-system 3: secondary imaging system, (b) DWP adjustment rings.

- (i) Theoretical calculation of structural parameters of DWP. The structural parameters of the DWP were determined through theoretical calculations, which primarily include its material, thickness, structural angle, and spacing.
- (j) Optical structure construction of DWP. Constructing an optical structure in optical design software based on the theoretical calculation parameters in step (i).
- (k) Combination of Sub-systems. The combined system is constructed sequentially, beginning with the telescope objective, followed by the eyepiece, DWP, and secondary imaging systems. Ultimately, light from an infinitely distant object plane passes through these subsystems in succession and converges on the image plane.

3.2. Design and optimization of Sub-system1: Telescope objective system

The optimization design example for telescope objective system is provided. The main structure and telecentric constraints in CODE V during the optimization process can be expressed by:

$$\begin{cases} & \text{EFY SO..I} \ = \ 120 \\ & \text{Y F3 R1 SI} \ < \ = \ Y_{\text{max}} \\ & \text{MNE MNT MNA MAE 2} \\ & & \text{MXT 8} \\ & \text{AOI R1 SI F1} \ = \ 0 \\ & \text{AOI R1 SI F2} \ = \ 0 \\ & \text{AOI R1 SI F3} \ = \ 0 \end{cases}$$

where the first constraint is the effective focal length f of the telescopic objective system. The second constraint is the maximum actual imaging height Y_{max} at the image plane. The third constraint refers to the minimum element edge thickness, the minimum element center thickness, the minimum air center thickness, the minimum air edge thickness, and the fourth constraint is the maximum element center thickness. Additionally, other constraints are applied to ensure that the chief ray (R1) for each FOV (ranging from the central FOV F1 to the largest FOV F3) remains perpendicular to surface SI, thereby achieving telecentric imaging at SI.

The meridian plan view of the system is shown in Fig. 3(a). In this

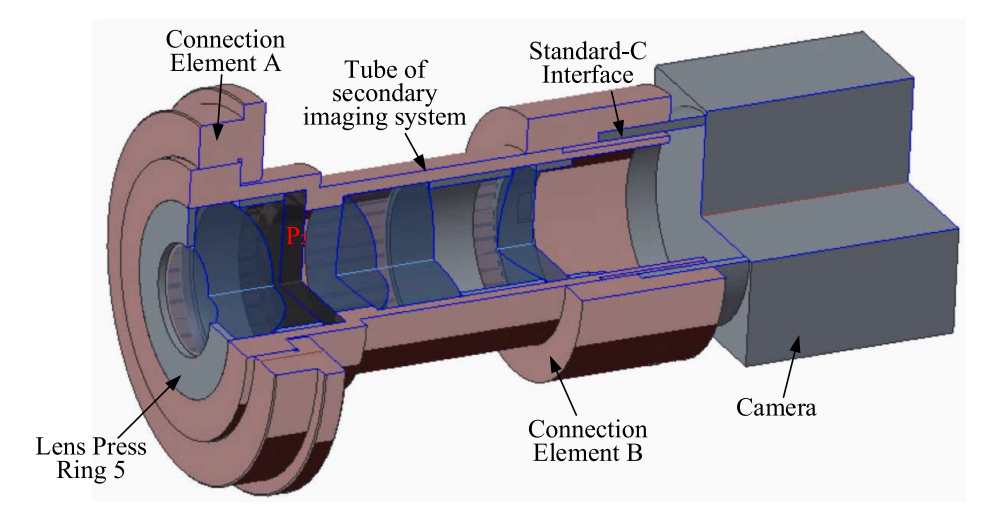


Fig. 14. Opto-mechanical structure of second imaging system which connecting with camera.

configuration, R₁ is oriented at 45° relative to the positive y-axis with a thickness of 4.85 mm, while R_2 is aligned at 90° to the y-axis with a thickness of 9.7 mm, and the polarizer P₁ is positioned at 45° to the yaxis with a thickness of 8 mm. Parallel light from a far-field target passes through the system and is finally focused onto the image plane SI, where the image height reaches 10.41 mm and the exit pupil diameter of 103.78 mm. The effective focal length f of the system is 119.99 mm, with a half FOV is 5°. The geometric spot diagram in Fig. 3(b) reveals small, consistently sized spots across various FOVs, indicating high-quality optical imaging. The distortion grid of the optimized telescope objective system is shown in Fig. 3(c), where the maximum distortion rate is nearly 0.5 %. The MTF of the optimized telescope objective system is given in Fig. 3(d). The edge-FOV MTF exceeds 0.6 at a spatial frequency of 60 cycles/mm. In addition, the field curves and distortion curves of the system are given in Fig. 3(e), which quantitatively reflect that the telescope objective system has smaller multi-wavelength field curvature and distortion. The structure and surface parameters of the optimized telescope objective system are shown in Table 2.

3.3. Design and optimization of Sub-system2: Eyepiece system

An example of the optimized eyepiece system design is presented, with the eyepiece system configured in reverse. To maximize the confinement of the beam within a specific lens aperture and mitigate image quality deterioration stemming from excessively large apertures, the pupil diameter has been set to 5.00 mm. During the optimization process, the main structural and telecentric constraints of CODE V can be expressed as follows:

The main point here is that the second constraint is to ensure that the image height of the eyepiece system is equal to the image height of the telescope objective system.

The meridional plan view of the eyepiece system is shown in Fig. 4 (a). The eyepiece consists of a double cemented lens and a single lens. Parallel light passes through the system and is finally focus onto the image plane SI, where the image height reaches 10.40 mm and the exit pupil diameter is 102.70 mm. The system features an effective focal length f of 40.01 mm and a half FOV of 15°. The geometric spot diagram

in Fig. 4(b) shows the presence of small and consistently sized spots across various FOVs, ensuring high-quality optical imaging. The distortion grid for the optimized eyepiece system is shown in Fig. 4(c), where the maximum distortion rate is nearly 0.1 % for better imaging. The MTF of the optimized eyepiece system is given in Fig. 4(d). The edge-FOV MTF exceeds 0.4 at a spatial frequency of 60 cycles/mm, indicating the capability to deliver high-quality imaging. The field curves and distortion curves of the system are given in Fig. 4(e), which quantitatively reflect the eyepiece system's field curvature and distortion. The structure and surface parameters of the optimized eyepiece system are shown in Table 3.

3.4. Design and optimization of Sub-system3: Secondary imaging system

An example of design optimization of the optical system of a secondary imaging system is provided. In the optimization process, the main constraints of CODE V can be expressed as follows:

$$\begin{cases}
EFY SO.I = 50 \\
MNE MNT MNA MAE 2 \\
MXT 8
\end{cases}$$
(16)

The main consideration for this system is just to constrain the effective focal length. Also set its pupil diameter equal to the eyepiece system.

A meridional plan view of the system is shown in Fig. 5(a), where the polarizer P_2 is oriented at 45° to the y-axis with a thickness of 8 mm. The system has an effective focal length f of 50.01 mm and a half FOV of 15° . The geometrical spot diagram in Fig. 5(b) shows the presence of small and consistently sized spots across various FOVs, ensuring high-quality optical imaging. The distortion grid of the optimized secondary imaging system is shown in Fig. 5(c), where the maximum distortion rate is close to 0.5 % barrel distortion. The MTF of the system is given in Fig. 5(d), where the edge-FOV MTF exceeds 0.4 at a spatial frequency of 60 cycles/mm, indicating minimal aberration and high image clarity. The field curves and distortion curves of the system are given in Fig. 5(e), which quantitatively reflect that the secondary imaging system has smaller field curvature and distortion. The structure and surface parameters of the optimized secondary imaging system are shown in the Table 4.

3.5. Design and optimization of FTSPIS

(1) Principle analysis of light split

The DWP is constituted by two identical Wollaston prisms WP1 and WP2 with an adjustable air gap of width *s* between them, as shown in Fig. 6. A Wollaston prism (WP) is formed by two uniaxial wedge-shaped

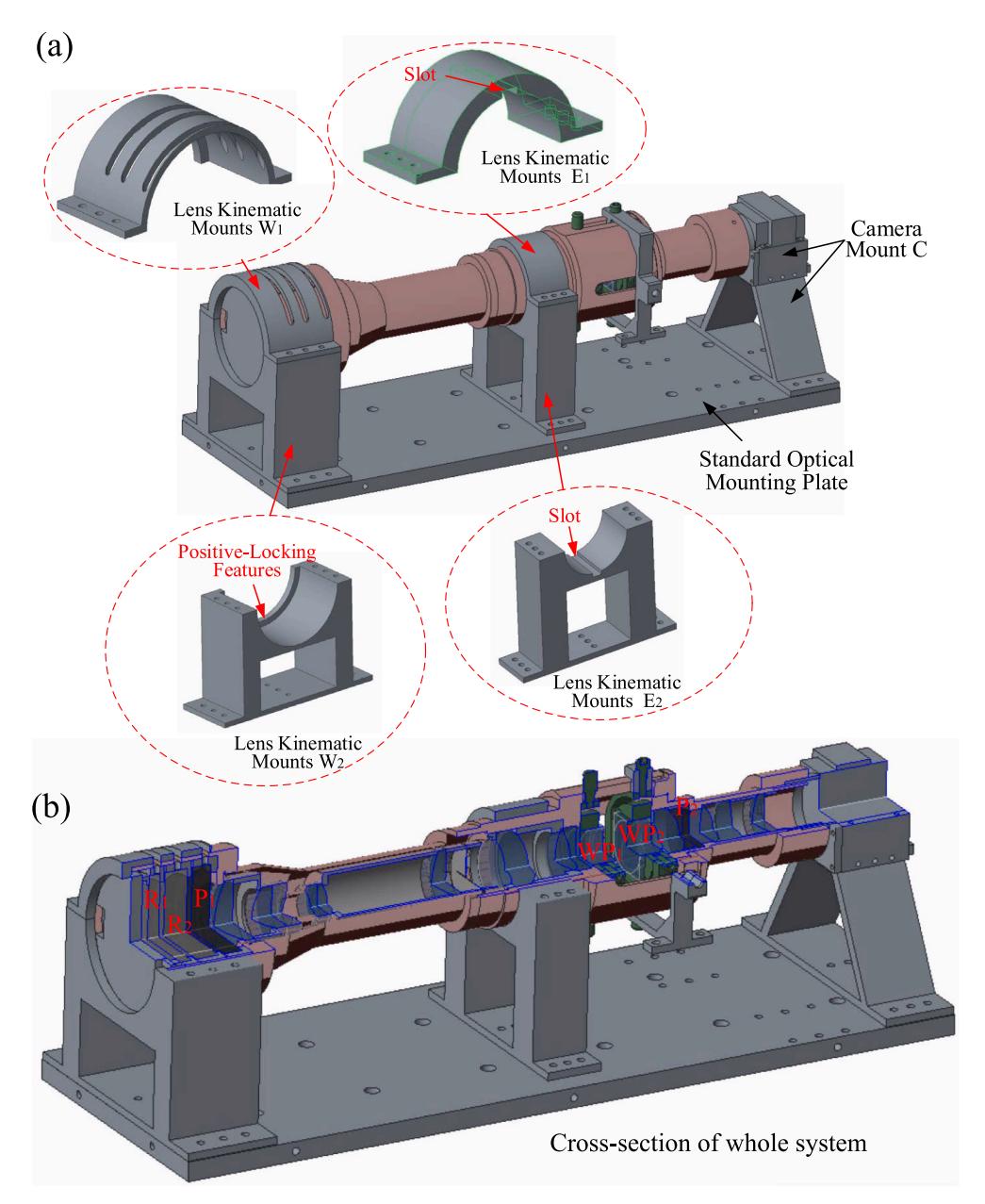


Fig. 15. Overall mechanical structure with (a) some lens system fixing structures: Lens fixing structures W₁, W₂, E₁, E₂ and structure C, (b) cross section view of whole opto-mechanical system.

crystals with mutually perpendicular optical axes, defined by the structure angle β and the plate thickness t.

When an incident wave passes through the DWP, it splits into two waves with orthogonal polarization states and parallel propagation directions. Fig. 6 illustrates the schematic diagram showing wave propagation through the DWP. Due to the perpendicular optic axes of the two wedge-shaped crystals of WP, their principal sections are oriented at right angles to each other. Consequently, a wave that behaves as an ordinary wave in the first crystal becomes an extraordinary wave in the second crystal, and vice versa. After passing through the DWP, the normal incident wave can be split into two parallel waves o (red) and e (blue).

(2) Optimization and analysis of FTSPIS

The primary constraints encountered during the execution of the system optimization process are given as follows:

$$\begin{cases} & \text{EFY S0..18} = 120 \\ & \text{EFY S19..24} = 40 \\ & \text{EFY S30..I} = 50 \\ & \text{MNE MNT MNA MAE 2} \\ & \text{MXT 8} \\ & \text{Y F3 R1 SI} > -15.00 < -14.00 \end{cases} \tag{17}$$

The first three constraints are implemented to ensure that the effective focal length f emains consistent across all subsystems throughout the optimization process. The final constraint governs the image height, as the back focal plane is interfaced with a CMOS camera featuring an element size of 5.5 μm .

```
\left\{ \begin{array}{l} Y\,F1\,S18\,R1 = Y\,F1\,S18\,R2 = Y\,F1\,S18\,R3 = Y\,F1\,S18\,R4 = Y\,F1\,S18\,R5 \\ Y\,F2\,S18\,R1 = Y\,F2\,S18\,R2 = Y\,F2\,S18\,R3 = Y\,F2\,S18\,R4 = Y\,F2\,S18\,R5 \\ Y\,F3\,S18\,R1 = Y\,F3\,S18\,R2 = Y\,F3\,S18\,R3 = Y\,F3\,S18\,R4 = Y\,F3\,S18\,R5 \\ THI\,S17 > 30 \\ THI\,S18 > 20 \end{array} \right.
```

(18)

The first three constraints are ensured the capability for normal imaging at the S18, thereby ensuring the interchangeability of the telescope objective system. The following two constraints are crucial for providing sufficient space both in front of and behind S18, allowing for the integration of a slit or FOV diaphragm during experiments phases.

As Fig. 7(a) shows the meridional plan view of the FTSPIS after connecting and optimizing all Sub-systems. In the figure, S18 represents the first image plane, and the parallel light is focused onto SI after passing through the complete system, resulting in an image height of 14.01 mm. Fig. 7(b) illustrates the separation of the chief ray of 0° and 5° incidence. Fig. 7(c) gives the MTF of the optimized system, and the image resolution of the system is better when the Nyquist frequency is taken. The geometric spot diagram in Fig. 7(d) shows the presence of close sized spots across different FOVs, ensuring high-quality imaging. The field curves and distortion curves are given in Fig. 7(e) and it is seen that there is about 1.7 % barrel distortion in the system. Finally, the structural and surface parameters of the optimized system are detailed in Table 5.

4. Simulation of the FTSPIS

In Section 2, we introduce the principles underlying polarization modulation and interference modulation. Based on the principles, we designed a computer simulation experiment to model the process of recovering spectral and polarization information.

First, we generated the Stokes parameters for the incident light. The parameters S_0 , S_1 , and S_3 were computed using a one-dimensional interpolation function, while S_2 was derived from the relationship S_2 = S_0 - $(S_1 + S_3)/2$. The resulting original spectrum is shown in Fig. 8.

In Fig. 8, S0 represents the total light intensity, S_1 indicates the difference in intensity between the horizontal and vertical polarization components, S_2 reflects the difference in intensity between the 45° and 135° polarization components, and S_3 represents the difference in intensity between the right-handed and left-handed circular polarization components.

Subsequently, the original spectrum underwent polarization modulation based on the mathematical principles governing the polarization modulation module. After polarization modulation, the total light intensity S_0 contains information from the original signal components S_0 through S_3 , and its intensity curve is shown in Fig. 9.

As shown in Fig. 9, the black curve represents the modulated spectral intensity, which includes all Stokes parameter information of the incident light, with each Stokes parameter modulated at a different carrier frequency. The emitted light undergoes interference modulation, resulting in a seven-channel interference intensity curve, as shown in Fig. 10.

Finally, channel filtering is applied to extract the C_0 , C_1 , and C_2 interference pattern channels. This is followed by Fourier transformation and demodulation of the polarization information to recover the Stokes parameters. The recovery results are shown in Fig. 11.

Compared to Fig. 8, all four Stokes parameters of the incident light have been effectively recovered. The recovery is particularly accurate in the central wavelength band, while there is a slight decrease in accuracy at both ends of the spectrum. This is primarily due to information loss caused by the truncation of the interferogram and the Gibbs phenomenon resulting from the Fourier transform. However, this does not affect the recovery of the main spectral and polarization information in practical applications. Therefore, the simulation results demonstrate the feasibility of the FTSPIS.

5. Overall opto-mechanical structure for PIIS

5.1. Opto-mechanical structure for telescopic objective system

As shown in Fig. 12, the opto-mechanical structure for telescopic objective system is illustrated through cross-section schematics. The

design incorporates three kinematic mounting interfaces within Lens Assembly Rings to enable independent rotational control of phase retarders R_1 , R_2 , and polarizer P_1 . The lens rotation adjustment slots in the lens tube and the screw holes on the Lens Assembly Rings are also designed. Lens Front Cover is an optical lens protective cover (screwthread mounted and dismountable). Lens Spacer 1 and Lens Spacer 2 are a kind of annular structure used to precisely fix two lenses with a certain air gap in the lens tube.

During the system testing and alignment process, precise adjustment of the phase retarders $(R_1,\ R_2)$ and polarizer (P_1) can be achieved through individual rotation of their respective mounting screws along the designated slots. The telescopic objective system incorporates a removable slit plate in its imaging plane (SI) to facilitate different operational modes: the slit plate, secured by Lens Press Ring 3 and Lens Press Ring 4, can be installed for slit imaging spectral analysis or removed for full-FOV imaging applications. In terms of opto-mechanical integration, our design implements a stringent tolerance of \pm 0.01 mm for the alignment between imaging optical components and their corresponding mechanical structures, ensuring optimal system performance and precision.

5.2. Opto-mechanical structure for eyepiece system and DWP assembly system

As depicted in Fig. 13, the opto-mechanical structure for the eyepiece system and DWP Assembly has been designed to resolve critical alignment challenges. A persistent challenge in WP fabrication involves the inherent difficulty of achieving high-precision alignment between the geometric optical axis of the lens and the crystal axis. Manufacturing tolerances introduce misalignment errors, which severely restrict the application of WPs in high-performance optical systems, such as spectral interference system. To address this, the DWP Assembly incorporates both angular adjustment and translational compensation functionalities. The cross-sectional schematic in Fig. 13(a) illustrates the overall system structure, with the DWP Assembly highlighted in green detailed in Fig. 13(b). A motorized translational push rod, driven by a stepper motor providing 0.02 mm positioning accuracy, facilitates controlled axial displacement of WP2 along the optical Z-axis, ensuring micronlevel alignment accuracy.

As shown in Fig. 13(b), the dual-degree-of-freedom adjustment mechanism (prism angle and translation) is exemplified through WP₁ alignment. The WP Assembly comprises four core components: an inner ring for WP mounting, an outer ring, and two adjustment Screw A and Screw B. The inner ring interfaces with the outer ring via precision-ground contact surfaces at their left/right outer and inner end faces, respectively. Rotational adjustment of WP₁ in the α -direction is achieved by actuating Screw A, while β -axis rotation is controlled through coordinated manipulation of Screw A and the right-end screw along the tube groove. Following angular alignment, translational positioning of the WP₁ assembly can be realized by sliding the along the upper and lower inner walls of the tube or displacing the left/right screws within their respective slots. Final mechanical fixation is accomplished by tightening Screw B to secure the adjusted WP₁ assembly to the tubular outer wall.

5.3. Opto-mechanical structure for second imaging system

Fig. 14 shows the 3D opto-mechanical design of the secondary imaging system. As shown in the figure, the structure integrates two critical interfaces: Connection Element A for rigid coupling with the eyepiece splitting module, and Connection Element B for integration of Standard-C-Interface camera. To enable polarization axis alignment, the tube part of the system can be rotated as a whole (Connection Element A and Connection Element B are smoothly nested with the tube). In addition, axial displacement of the tubular housing along the optical axis facilitates co-planar alignment between the actual focal plane and the imaging sensor surface, with a controlled travel range for fine focal

position calibration. Final system stabilization is achieved through locking screws on both connection elements, ensuring rigid fixation after completion of focal plane positioning and polarization orientation adjustment.

5.4. Overall mechanical structure

Fig. 15 shows the 3D diagram of the final opto-mechanical structure of the proposed FTSPIS system. As shown in Fig. 15(a), in order to achieve the stability of the system in various environments, the kinematic mounts are designed to hold the entire system in place. The Lens Kinematic Mounts W_1 and W_2 are used to fix the front telescopic system of the FTSPIS system. W2 integrates Positive-Locking Features to eliminate forward displacement while suppressing off-axis motion through radial constraint. In addition, the Lens Kinematic Mounts E_1 and E_2 provide rigid fixation for the eyepiece beam-splitting subsystem, employing a constrained kinematic interface to prevent axial translation along the optical Z-axis and mitigate lateral misalignment. This dual retention strategy employs anti-rotation mechanisms and precision-guided interfaces, ensuring dimensional stability under operational stresses while maintaining optical alignment integrity.

The non-rotationally symmetric structure of the WP necessitates precision alignment. Owing to the slot design on the Lens Kinematic Mounts E_1 and E_2 , these constrained interfaces enforce proper tubular orientation while ensuring angular registration between the WP and the optical axis. The camera Mount C provides rigid kinematic coupling to the imaging sensor, ensuring precise optical axis alignment. The Standard Optical Mounting Plate serves dual purposes: (1) mechanical fixation of the entire system to optical breadboards for simplified testing integration, and (2) stabilization of the translational driving stepper motor for WP $_2$. As shown in Fig. 15(b), a cross-section view of the whole FTSPIS system is shown. The total length is less than 350 mm and the total weight is about 6 kg (considering the mechanical and optical materials). This optimized mass-volume profile enables deployment in airborne detection systems and unmanned aerial vehicle (UAV) platforms requiring high-precision spectral imaging capabilities.

6. Conclusion and prospect

This study presents an opto-mechanical design method of FTSPIS based on dual Wollaston prisms. Based on the basic working principle and theoretical basis of the spectral polarization interferometric imaging, a polarization interference system is divided into three independent modules: telescopic objective lens, eyepiece and splitting system, and secondary imaging system. The optimization design method of each module is introduced separately, the optical effect and the matching relationship between different modules are also presented. The design example realized a visible-spectrum FTSPIS with a full field of view (FOV) \pm 5°. The proposed design of FTSPIS is verified by the simulation analysis of interference and the demodulation. Furthermore, the corresponding mechanical structures and their functions for different modules are also presented. The mechanical structures are proposed for realizing a rotation angle adjustment for each lens of the phase modulation module (PMM). The mechanical structures are also proposed for realizing both the rotation angle and the translation adjustment of each Wollaston prism individually. The high precision adjustment with multiple degrees of freedom ensures that the system can achieve the predetermined optical effect.

This study mainly provides the design method, we give a design example to illustrate the overall design method of the system, analysis and simulation verify that the system has achieved a pretty optical effect. We hope that this work can provide some design ideas and engineering practice references for people in related fields. According to the proposed design method, the system has been designed and implemented. While this work primarily focuses on the design methodology and performance of the system, it is important to acknowledge that

practical implementation may introduce potential sources of error. Factors such as manufacturing tolerances, misalignments during assembly, and environmental variations (e.g., temperature and vibrations) could influence the system's performance. A detailed error analysis was intentionally excluded from this study to maintain the focus on the design principles.

In future work, these potential error factors can be rigorously analyzed and quantified through simulation and experimental validation. For instance, tolerancing analysis could be performed to evaluate the sensitivity of the system to optical component misalignments, and finite element modeling could assess the impact of mechanical deformations under operational conditions. Addressing these aspects will further enhance the robustness and reliability of the proposed design, making it suitable for broader real-world applications. As part of our future work, the design case presented in this study will be used to consider the processing of the optical lens and mechanical structure, along with installation and verification.

Declaration of competing interest

The authors declare that they have no known competing financial interests or personal relationships that could have appeared to influence the work reported in this paper.

Acknowledgments

This work is funded by National Natural Science Foundation Youth Science Foundation (62305263). We would like to thank Xiangzhe Zhang for providing the principle and technical support.

Data availability

Data will be made available on request.

References

- M.R. Torr, D. Torr, Atmospheric spectral imaging, Science 225 (4658) (1984) 169–171.
- [2] P.D. Hammer, F.P.J. Valero, D.L. Peterson, W.H. Smith, Imaging interferometer for terrestrial remote sensing, SPIE 1993 (1937) 244–255.
- [3] F. Vagni, Survey of Hyperspectral and Multispectral Imaging Technologies, North Atlantic Treaty Organisation (2007).
- [4] N. Hagen, M.W. Kudenov, Review of snapshot spectral imaging technologies Opt, Eng 52 (9) (2013) 090901.
- [5] Q. Zhang, Y.J. Shang, S.Y. Qiao, Y.H. Guo, R.J. Zhong, M.B. Pu, Y.L. Ha, M. Y. Wang, J. Lei, F. Zhang, M.F. Xu, X.G. Luo, Broadband Rapid Polarization Manipulation and Imaging Based on Pancharatnam-Berry Optical Elements Laser Photon, Rev (2024) 8.
- [6] J.T. Scott, G. Dennis, C. David, S. Joseph, J. Tyo, Review of passive imaging polarimetry for remote sensing applications, Appl. Optics 45 (22) (2006) 5453–5469.
- [7] N. Takanori, J. Bahram, Object recognition by use of polarimetric phase-shifting digital holography, Opt. Lett 32 (15) (2007) 2146–2148.
- [8] S. Tominaga, A. Kimachi, Polarization imaging for material classification, Opt. Eng 47 (12) (2008) 123201–123214.
- [9] X.J. Yu, Y.B. He, J.Y. Xiong, F.H. Yu, H.S. Kwok, Design of polarization interference filters, Displays 23 (3) (2002) 145–149.
- [10] M. Ahmad, J.N. Li, H.W. Ma, J. Liu, Ultrathin metasurface for super multi-view 3D display with linear and circular polarization control, Displays 85 (2024) 102848.
- [11] Y. Zhang, H.S. Li, J.H. Sun, X. Zhang, Z.M. Ling, Dual-dispersive spectral linear polarization imager based on coded-aperture, Opt. Laser Technol 170 (2024) 110149.
- [12] C.P. Chen, X. Wu, J. Wang, B. Han, Y. Yang, S. Liu, Penta-channel waveguide-based near-eye display with two-dimensional pupil expansion, Displays 88 (2025) 102999.
- [13] F. Zhang, M.H. Liao, M.B. Pu, Y.H. Guo, L.W. Chen, X. Li, Q. He, T.T. Kang, X.L. Ma, Y. Ke, X.G. Luo, A Miniature Meta-Optical System for Reconfigurable Wide-Angle Imaging and Polarization-Spectral Detection, Engineering 35 (2024) 67–73.
- [14] J.L. Ning, Z.L. Xu, D. Wu, R. Zhang, Y.Y. Wang, Y.G. Xie, W. Zhao, W.Y. Ren, Compressive circular polarization snapshot spectral imaging, Opt. Commun 491 (2021) 126946.
- [15] X.B. Li, L. Yan, P.F. Qi, L.P. Zhang, F. Goudail, T.G. Liu, J.S. Zhai, H.F. Hu, Polarimetric Imaging via Deep Learning: A Review, Remote Sens-Basel 15 (6) (2023) 1540.

- [16] H.X. Li, J.P. Zhu, J.X. Deng, F.Q. Guo, N. Zhang, J. Sun, X. Hou, Underwater active polarization descattering based on a single polarized image, Opt. Express 31 (13) (2023) 21988–22000.
- [17] M. Dubreuil, P. Delrot, I. Leonard, A. Alfalou, C. Brosseau, A. Dogariu, Exploring underwater target detection by imaging polarimetry and correlation techniques, Appl. Optics 52 (5) (2013) 997–1005.
- [18] K.O. Amer, M. Elbouz, A. Alfalou, C. Brosseau, J. Hajjami, Enhancing underwater optical imaging by using a low-pass polarization filter, Opt. Express 27 (2) (2019) 621–643
- [19] Y. Wei, P.L. Han, F. Liu, X.P. Shao, Enhancement of underwater vision by fully exploiting the polarization information from the Stokes vector, Opt. Express 29 (14) (2021) 22275–22287.
- [20] L.B. Wang, B. Zhang, Q. Shen, Y. Yao, S.Y. Zhang, H.D. Wei, R.P. Yao, Y.W. Zhang, Estimation of soil salt and ion contents based on hyperspectral remote sensing data: A case study of baidunzi basin, China. Water 13 (4) (2021) 559.
- [21] A. Singh, Soil salinization management for sustainable development: A review, J Environ Manage 277 (2021) 111383.
- [22] L. Guanter, C. Frankenberg, A. Dudhia, P.E. Lewis, J. Gómez-Dans, A. Kuze, H. Suto, R.G. Grainger, Retrieval and global assessment of terrestrial chlorophyll fluorescence from GOSAT space measurements, Remote Sens Environ 121 (2012) 225 251
- [23] S.H. Zhao, M. Liu, M.H. Tao, W. Zhou, X.Y. Lu, Y.J. Xiong, F. Li, Q. Wang, The role of satellite remote sensing in mitigating and adapting to global climate change, Sci Total Environ 904 (2023) 166820.
- [24] G. van Harten, J. de Boer, J.H.H. Rietjens, A. Di Noia, F. Snik, H. Volten, J.M. Smit, O.P. Hasekamp, J.S. Henzing, C.U. Keller, Atmospheric aerosol characterization with a ground-based SPEX spectropolarimetric instrument, Atmos Meas Tech 7 (12) (2014) 4341–4351.
- [25] H.J. Hoeijmakers, M.L.J. Arts, F. Snik, C.U. Keller, J.M. Kuiper, Design trade-off and proof of concept for LOUPE, the Lunar Observatory for Unresolved Polarimetry of Earth, Opt. Express 24 (19) (2016) 21435–21453.
- [26] J.W. Frost, F. Nasraddine, J. Rodriguez, I. Andino, B. Cairns, A handheld polarimeter for aerosol remote sensing, SPIE 5888 (2005) 269–276.
- [27] R.S. Gurjar, V. Backman, L.T. Perelman, I. Georgakoudi, K. Badizadegan, I. Itzkan, R.R. Dasari, M.S. Feld, Imaging human epithelial properties with polarized lightscattering spectroscopy, Nat Med 7 (11) (2001) 1245–1248.
- [28] R. Patel, A. Khan, R. Quinlan, A.N. Yaroslavsky, Polarization-sensitive multimodal imaging for detecting breast cancer, Cancer Res 74 (17) (2014) 4685–4693.
- [29] S. Magalhães, B.J. Goodfellow, A. Nunes, FTIR spectroscopy in biomedical research: How to get the most out of its potential, Appl Spectrosc Rev 56 (8–10) (2021) 869–907.
- [30] I. Delfino, V. Ricciardi, M. Lepore, Synchrotron FTIR microspectroscopy investigations on biochemical changes occurring in human cells exposed to proton beams. Appl Sci-Basel 12 (1) (2022) 336.
- [31] V. Neto, S. Esteves-Ferreira, I. Inacio, M. Alves, R. Dantas, I. Almeida, J. Guimarães, T. Azevedo, A. Nunes, Metabolic profile characterization of different thyroid nodules using FTIR spectroscopy: a review, Metabolites 12 (1) (2022) 53.
- [32] A. Huete, G. Ponce-Campos, Y.G. Zhang, N. Restrepo-Coupe, X.L. Ma, M. Moran, Monitoring photosynthesis from space, CRC Press, 2015, p. 20.
 [33] D. Haboudane, J.R. Miller, E. Pattey, P. Zarco-Tejada, I. Strachan, Hyperspectral
- [33] D. Haboudane, J.R. Miller, E. Pattey, P. Zarco-Tejada, I. Strachan, Hyperspectral vegetation indices and novel algorithms for predicting green LAI of crop canopies: Modeling and validation in the context of precision agriculture, Remote Sens Environ 90 (3) (2004) 337–352
- [34] W.Q. Huang, J.B. Li, Q.Y. Wang, L.P. Chen, Development of a multispectral imaging system for online detection of bruises on apples, J Food Eng 146 (2015) 62–71
- [35] Y.S. Lei, Q. Zhang, Y.H. Guo, M.B. Pu, F. Zou, X. Li, X.L. Ma, X.G. Luo, Snapshot multi-dimensional computational imaging through a liquid crystal diffuser, Phot Res 11 (03) (2023) 350–363.
- [36] H.Y. Zhu, B.Q. Chu, C. Zhang, F. Liu, L.J. Jiang, Y. He, Hyperspectral imaging for presymptomatic detection of tobacco disease with successive projections algorithm and machine-learning classifiers, Sci Rep 7 (1) (2017) 4125.
- [37] H. Gao, X.H. Fan, Y.X. Wang, Y.C. Liu, X.E. Wang, K. Xu, L.M. Deng, C. Zeng, T. A. Li, J.S. Xia, W. Xiong, Multi-foci metalens for spectra and polarization ellipticity recognition and reconstruction, OES 2 (03) (2023) 11–21.

- [38] C. Chen, X.Y. Li, G. Yang, X.H. Chen, S.P. Liu, Y.H. Guo, H. Li, Computational hyperspectral devices based on quasi-random metasurface supercells, Nanoscale 15 (19) (2023) 8854–8862.
- [39] N. Gupta, Development of Spectropolarimetric Imagers from 400 to 1700 nm, SPIE 9099 (2014) 165–175.
- [40] K. Oka, T. Kato, Spectroscopic polarimetry with a channeled spectrum, Appl. Optics 24 (21) (1999) 1475–1477.
- [41] J.F. Iannarilli, S. Jones, H. Scott, P. Kebabian, Polarimetric-spectral intensity modulation (P-SIM): enabling simultaneous hyperspectral and polarimetric imaging, SPIE 3698 (1999) 474–481.
- [42] M. Escuti, C. Oh, C. Sánchez, C. Bastiaansen, D. Broer, Simplified spectropolarimetry using reactive mesogen polarization gratings, SPIE 6302 (2006) 21 21
- [43] T. Okamoto, I. Yamaguchi, Simultaneous acquisition of spectral image information, Opt Lett 16 (16) (1991) 1277–1279.
- [44] M.R. Descour, C.E. Volin, E.L. Dereniak, T.M. Gleeson, M.F. Hopkins, D.W. Wilson, P.D. Maker, Demonstration of a computed-tomography imaging spectrometer using a computer-generated hologram disperser, Appl. Optics 36 (16) (1997) 3694–3698.
- [45] R.W. Aumiller, N. Hagen, E.L. Dereniak, R. Sampson, R. McMillan, Design of an LWIR snapshot imaging polarization spectrometer, SPIE 6295 (2006) 96–104.
- [46] R.W. Aumiller, C. Vanderlugt, E.L. Dereniak, R. Sampson, Snapshot imaging spectropolarimetry in the visible and infrared, SPIE 6972 (2008) 99–107.
- [47] J. Bo, Y.X.Z. Gu, W.H. Xing, X.P. Ju, C.X. Yan, X.D. Wang, Spatially modulated snapshot computed tomographic polarization imaging spectrometer, Appl. Optics 60 (20) (2021) 5860–5866.
- [48] T. Tsai, D. Brady, Coded aperture snapshot spectral polarization imaging, Appl. Optics 52 (10) (2013) 2153–2161.
- [49] C. Fu, H. Arguello, B. Sadler, G. Arce, Compressive spectral polarization imaging by a pixelized polarizer and colored patterned detector, J Opt Soc Am A 32 (11) (2015) 2178–2188.
- [50] W.Y. Ren, C. Fu, D. Wu, Y.G. Xie, G. Arce, Channeled compressive imaging polarization spectrometer, Opt. Express 27 (3) (2019) 2197–2211.
- [51] Z.Y. Chen, C.M. Zhang, T.K. Mu, T.Y. Yan, D.H. Bao, Z.Y. Chen, Y.F. He, Coded aperture snapshot linear-Stokes imaging polarization spectrometer, Opt. Commun 450 (2019) 72–77.
- [52] Z.Y. Chen, C.M. Zhang, T.K. Mu, Y. Wang, Y.F. He, T.Y. Yan, Z.Y. Chen, Coded aperture full-stokes imaging polarization spectrometer, Opt. Laser Technol 150 (2022) 107946.
- [53] T.K. Mu, C.M. Zhang, C. Jia, W. Ren, Static hyperspectral imaging polarimeter for full linear Stokes parameters, Opt. Express 20 (16) (2012) 18194–18201.
- [54] C.X. Bai, J.X. Li, Y. Shen, J. Zhou, Birefringent Fourier transform imaging spectrometer with a rotating retroreflector, Opt. Lett 41 (15) (2016) 3647–3650.
- [55] Q. Liu, C.X. Bai, J. Liu, J.L. He, J.X. Li, Fourier transform imaging polarization spectrometer using ferroelectric liquid crystals and Wollaston interferometer, Opt. Express 25 (17) (2017) 19904–19922.
- [56] T.Y. Yan, C.M. Zhang, J.R. Zhang, N.C. Quan, C.C. Tong, High resolution channeled imaging spectropolarimetry based on liquid crystal variable retarder, Opt. Express 26 (8) (2018) 10382–10391.
- [57] Q. Li, F. Lu, X. Wang, C. Zhu, Low crosstalk polarization-difference channeled imaging polarization spectrometer using double-Wollaston prism, Opt. Express 27 (8) (2019) 11734–11747.
- [58] C.X. Bai, J.X. Li, W.F. Zhang, Y.X. Xu, Y.T. Feng, Static full-Stokes Fourier transform imaging polarization spectrometer capturing spectral, polarization, and spatial characteristics, Opt. Express 29 (23) (2021) 38623–38645.
- [59] X.Z. Zhang, J.P. Zhu, L.Q. Huang, Y. Zhang, H.M. Wang, H.X. Li, F.Q. Guo, J. X. Deng, Hyperspectral channel-modulated static birefringent fourier transform imaging polarization spectrometer with zoomable spectral resolution, Photonics 10 (8) (2023) 950.
- [60] X.Z. Zhang, L.Q. Huang, J.P. Zhu, N. Zhang, K. Zong, L.P. Zhai, Y. Zhang, Y.K. Cai, H.M. Wang, Exact optical path difference and complete performance analysis of a spectral zooming imaging spectrometer, Opt. Express 30 (22) (2022) 39479–39491.